PAPER • OPEN ACCESS

The impact of motion on onboard MRI-guided pencil beam scanned proton therapy treatments

To cite this article: Alisha Duetschler *et al* 2024 *Phys. Med. Biol.* **69** 095003

IOP Publishing Phys. Med. Biol. 69 (2024) 095003 https://doi.org/10.1088/1361-6560/ad3885

Physics in Medicine & Biology

IPEM Institute of Physics and Engineering in Medicine

OPEN ACCESS

RECEIVED
9 October 2023

REVISED
11 March 2024

ACCEPTED FOR PUBLICATION
26 March 2024

PUBLISHED
15 April 2024

PAPER

The impact of motion on onboard MRI-guided pencil beam scanned proton therapy treatments

Alisha Duetschler[1,2], **Sairos Safai**[1], **Damien C Weber**[1,3,4], **Antony J Lomax**[1,2] **and Ye Zhang**[1]

[1] Center for Proton Therapy, Paul Scherrer Institute, 5232 Villigen PSI, CH, Switzerland
[2] Department of Physics, ETH Zürich, 8092 Zürich, CH, Switzerland
[3] Department of Radiation Oncology, University Hospital of Zürich, 8091 Zürich, CH, Switzerland
[4] Department of Radiation Oncology, Inselspital, Bern University Hospital, University of Bern, 3010 Bern, CH, Switzerland

E-mail: ye.zhang@psi.ch

Keywords: MR-guidance, proton therapy, 4D dose calculation, intra-fraction motion, lung tumour, liver tumour

Abstract

Objective. Online magnetic resonance imaging (MRI) guidance could be especially beneficial for pencil beam scanned (PBS) proton therapy of tumours affected by respiratory motion. For the first time to our knowledge, we investigate the dosimetric impact of respiratory motion on MRI-guided proton therapy compared to the scenario without magnetic field. *Approach.* A previously developed analytical proton dose calculation algorithm accounting for perpendicular magnetic fields was extended to enable 4D dose calculations. For two geometrical phantoms and three liver and two lung patient cases, static treatment plans were optimised with and without magnetic field (0, 0.5 and 1.5 T). Furthermore, plans were optimised using gantry angle corrections (0.5 T +5° and 1.5 T +15°) to reproduce similar beam trajectories compared to the 0 T reference plans. The effect of motion was then considered using 4D dose calculations without any motion mitigation and simulating 8-times volumetric rescanning, with motion for the patient cases provided by 4DCT(MRI) data sets. Each 4D dose calculation was performed for different starting phases and the CTV dose coverage $V_{95\%}$ and homogeneity $D_{5\%}$–$D_{95\%}$ were analysed. *Main results.* For the geometrical phantoms with rigid motion perpendicular to the beam and parallel to the magnetic field, a comparable dosimetric effect was observed independent of the magnetic field. Also for the five 4DCT(MRI) cases, the influence of motion was comparable for all magnetic field strengths with and without gantry angle correction. On average, the motion-induced decrease in CTV $V_{95\%}$ from the static plan was 17.0% and 18.9% for 1.5 T and 0.5 T, respectively, and 19.9% without magnetic field. *Significance.* For the first time, this study investigates the combined impact of magnetic fields and respiratory motion on MR-guided proton therapy. The comparable dosimetric effects irrespective of magnetic field strength indicate that the effects of motion for future MR-guided proton therapy may not be worse than for conventional PBS proton therapy.

1. Introduction

The use of online magnetic resonance imaging (MRI) has emerged as a groundbreaking approach in the field of radiotherapy-based cancer treatment, enabling the real-time visualization of the tumour and surrounding anatomy during the treatment delivery. MRI stands out as a non-ionizing imaging technique that offers exceptional soft-tissue contrast. For conventional photon radiotherapy, onboard MRI guidance is already in clinical use with two commercial systems (Mutic and Dempsey 2014, Raaymakers *et al* 2017).

Due to the dose deposition in sharp Bragg peaks (Bragg and Kleeman 1905), pencil beam scanned (PBS) proton therapy has the potential to deliver highly conformal dose distributions to the tumour while reducing the dose to nearby organs at risk (OARs) (Lomax *et al* 1999a) compared to conventional photon radiotherapy. On the other hand, protons are very sensitive to any variations in patient positioning and internal anatomical changes. As a result, accurate real-time image guidance becomes more essential and demanding to exploit the

benefits of proton therapy fully. Consequently, online MRI guidance for PBS proton therapy has been an active field of research and first prototype systems for MRI-guided proton therapy are being developed (Oborn *et al* 2017, Hoffmann *et al* 2020, Pham *et al* 2022).

As the particles are charged, however, the effect of the magnetic field on proton beam dose deposition has to be considered during the dose calculation and treatment planning. This has been investigated in various simulation studies using Monte Carlo (MC) simulations (Raaymakers *et al* 2008, Moteabbed *et al* 2014, Hartman *et al* 2015, Oborn *et al* 2015, Fuchs *et al* 2017, Kurz *et al* 2017, Burigo and Oborn 2019, Lühr *et al* 2019, Santos *et al* 2019, Burigo and Oborn 2021), while analytical or numerical approaches to account for the deflection of proton beams in a perpendicular magnetic field have also been proposed (Wolf and Bortfeld 2012, Hartman *et al* 2015, Fuchs *et al* 2017, Schellhammer and Hoffmann 2017) and integrated into analytical dose calculation algorithms by Padilla-Cabal *et al* (2018, 2020), Duetschler *et al* (2023b). Furthermore, results from the operation of experimental systems have been reported (Schellhammer *et al* 2018a, 2018b, Lühr *et al* 2019, Padilla-Cabal *et al* 2019, Gantz *et al* 2020, 2021, Fuchs *et al* 2022).

To date, however, only a limited number of treatment planning studies have investigated the clinical benefits associated with onboard MRI guidance for proton therapy. Moreover, these studies, which encompassed pediatric (Acharya *et al* 2020), liver (Moteabbed *et al* 2021a), prostate (Moteabbed *et al* 2021b), and lung cancer patients (Rabe *et al* 2023), did not consider the effect of the magnetic field on the proton dose distributions. In another study, Kurz *et al* (2017) used MC-based treatment planning to investigate the robustness against setup errors and anatomical changes for prostate treatment plans optimised with and without a magnetic field. None of these studies did, however, account for the deteriorating effects of motion on the delivered dose distributions, although lung and liver treatments are particularly susceptible to respiratory motion during the treatment delivery. On the other hand, these treatment sites are affected by respiratory motion and could eventually benefit from MRI guidance the most, as the real-time MR images could be used to gate the treatment or for tumour tracking.

Thus, for the future implementation of online MRI-guided proton therapy for moving tumours, the dose calculation should not only consider the impact of the magnetic field on the dose distributions, but also the effect of motion on the dose. Therefore, in this paper, a fast MR-compatible analytical dose calculation, as developed by Duetschler *et al* (2023b), has been extended to 4D dose calculations and used to perform, to our knowledge, first dosimetric simulations that consider the joint impact of respiratory motion and magnetic fields on PBS proton therapy. As such, and as a 'worst case' scenario, we investigate here the potential effect of unmitigated motions on MR-guided PBS plans, as well as the potential effectiveness of rescanning (arguably the simplest motion management technique) on such treatments. As motion-induced density changes in the beam path could influence not only the proton range but also the proton beam trajectory in the presence of a magnetic field, these results are also compared to reference cases without magnetic fields.

2. Materials and methods

2.1. 4D dose calculation considering magnetic field

The analytical dose calculation algorithm accounting for the deflection of the proton beams in a perpendicular homogenous magnetic field is described in detail in Duetschler *et al* (2023b) and we only provide a short description here. The dose calculation is based on ray casting (Schaffner *et al* 1999), which has been adjusted to account for the deflected beam trajectories. The deflected beam trajectories are determined through the utilization of look-up tables (LUTs) that consist of incremental rotation angles as a function of water-equivalent depth. Specifically, the trajectory is reconstructed iteratively, and in each step the direction is adjusted based on the rotation angle obtained from the LUT. These LUTs were generated from TOPAS MC (Perl *et al* 2012, Faddegon *et al* 2020) calculations of single pencil beams (70–229 MeV, 115 energies) in water in orthogonal magnetic fields (0.5/1.5 T). A validation of the algorithm against MC in different media and for patient cases is also presented in Duetschler *et al* (2023b).

In this work, this algorithm has been further extended to account for deformable motion and motion-induced density changes. The information about the motion and density changes is provided by a 4DCT, from which the motion is extracted in the form of deformation vector fields (DVFs) using deformable image registration (DIR). The first step, for 4D dose calculation, which simulates the interplay effect between the patient's motion and the dynamical beam delivery, is the calculation of the delivery time of each pencil beam. Based on the delivery time, the pencil beams are then assigned to the closest phase of the 4DCT. Considering the impact of the magnetic field as described above, the dose contributions to all phases are then calculated. The doses from all phases are finally warped according to the DVFs and accumulated on a reference phase. In this

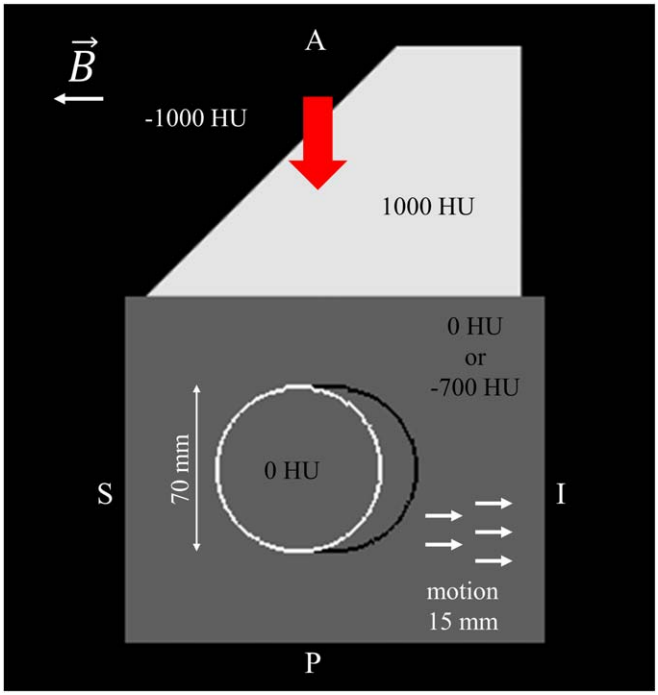

Figure 1. Phantom with high-density wedge (1000 HU) and spherical target (0 HU) surrounded by water (0 HU, Phantom A) or lung tissue (−700 HU, Phantom B). The CTV is delineated in white and the ITV in black. The direction of the proton beam is indicated by a red arrow.

work, DIRs were performed using a 3D multi-resolution B-spline registration with the open-source software Plastimatch[5] were employed.

2.2. Investigated cases

2.2.1. Geometrical phantoms

As a first check on the correctness of the developed 4D dose calculation algorithm, it was first applied to the two digital geometrical phantoms depicted in figure 1. Each phantom comprises a stationary high-density 45° wedge (1000 HU) and a spherical target with a diameter of 70 mm (0 HU). The sphere is positioned within either water (0 HU) or lung tissue (−700 HU), referred to as 'Phantom A' and 'Phantom B', respectively. In order to simulate respiratory motion, the spherical target and the surrounding material undergo rigid translation, while the wedge remains stationary. Specifically, a one-dimensional $\sin^4$ motion is applied in the superior-inferior (SI) direction, with an amplitude of 15 mm and a period of 5 s.

2.2.2. 4DCT(MRI) patient data sets

For three liver and two lung cancer patients, anatomy and density information is provided by their respective clinical 3DCTs. The 3DCTs for the liver patients were acquired during end exhalation (EE), whereas the lung 3DCTs were obtained during deep-inspiration breath-hold (DIBH) (Josipovic *et al* 2016). We also refer to these 3DCTs as reference phases. For investigating realistic irregular respiratory motion, the 3DCTs were animated with multiple breathing cycle motion extracted from 4DMRIs of healthy volunteers (von Siebenthal *et al* 2007, Jud *et al* 2018) to generate so-called 4DCT(MRI)s as described in Boye *et al* (2013a) for liver and Duetschler *et al* (2022) for lung. The used liver and lung CTs have a resolution of $1.96 \times 1.96 \times 2.5$ mm^3 and $1.96 \times 1.96 \times 2$ mm^3, respectively.

One volunteer 4DMRI consisting of 10 distinct breathing cycles, with a temporal resolution of 2.77 Hz, was used to generate the three liver 4DCT(MRI)s. In contrast, for the two lung 4DCT(MRI)s, a second 4DMRI comprising 15 breathing cycles, with a temporal resolution of 2.25 Hz, was utilized. The liver 4DMRI has a spatial resolution of $1.8 \times 1.8 \times 3$–4 mm^3 (von Siebenthal *et al* 2007), while the lung 4DMRI has a uniform voxel size of $3.125 \times 3.125 \times 3.125$ mm^3 (Duetschler *et al* 2022).

For every case and breathing cycle, we computed the median and 95th percentile motion amplitude across all voxels within the CTV. The resulting motion variability for the studied 4DCT(MRI)s is summarized in figure 2. For both indications, the differences in amplitude between the CT anatomies can be attributed to different

[5] https://plastimatch.org. Accessed August 30, 2023.

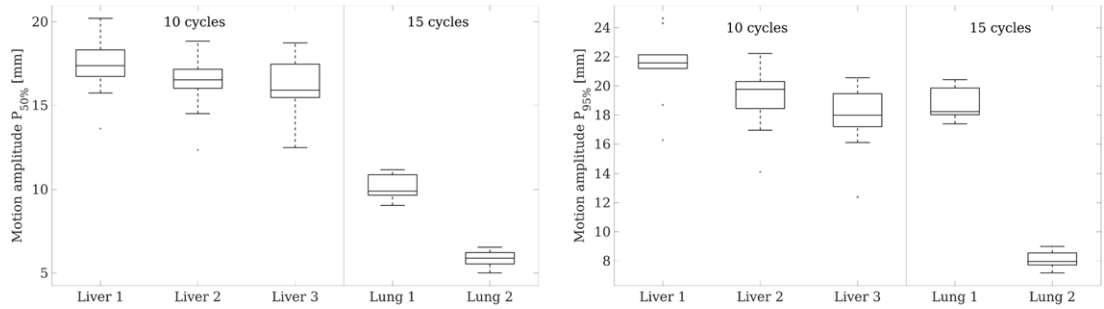

Figure 2. Median ($P_{50\%}$) and 95th percentile ($P_{95\%}$) values of motion amplitude within the CTV. Boxplots summarize results for 10 and 15 breathing cycles for liver and lung cases, respectively (a) Motion CTV $P_{50\%}$ (b) Motion CTV $P_{50\%}$.

tumour locations. The liver and lung 4DCT(MRI)s have an average period of 6.6 ± 0.8 s and 4.8 ± 0.4 s, respectively.

The same data was used to investigate uncertainties associated with PBS proton 4D dose calculation in Duetschler *et al* (2023a), where the data is described in more detail. Furthermore, the analytical dose calculation algorithm considering the impact of the magnetic field was validated against MC for the Liver 1 and Lung 1 cases in Duetschler *et al* (2023b).

2.3. Planning CT and target volume definition

For treatment plan optimisation, the clinical target volumes (CTV) of all phases of the first breathing cycle were combined to form the internal target volume (ITV). The ITV was further extended by a 2 mm margin to form the planning target volume (PTV) and ensure target coverage in the static case. For the planning CT, the mean intensity throughout the first breathing cycle was calculated for all voxels. However, for voxels in the ITV, the maximum intensity value was utilized, following the definition by Botas *et al* (2018).

2.4. Treatment planning

For simulating a patient lying in an MRI scanner, we assumed a uniform magnetic field within a cylindrical region surrounding the isocenter for all dose calculations and treatment plan optimisations. Like both commercially available photon MR-linac systems, a radius of 35 cm was assumed. Uniform field strengths of 0.5 T and 1.5 T were simulated and compared to the scenario without any magnetic field (0 T).

On the static planning CT, treatment plans were optimised as described in Duetschler *et al* (2023b) assuming magnetic field strengths of 0, 0.5 and 1.5 T. A single field (see figure 1) was selected for the geometrical phantoms, while simplified treatment plans with two fields were optimised using a single-field uniform-dose (SFUD) approach for the 4DCT(MRI) liver and lung cases. Furthermore, to correct for the different beam entrance and beam paths within the patient introduced by the magnetic field, additional treatment plans were optimised with gantry rotations of $+5°$ and $+15°$ for 0.5 T and 1.5 T, respectively. This resulted in similar beam paths within the patient as compared to the scenario without any magnetic field. Plans were optimized with a 2.5 mm distal and 4 mm lateral spot spacing.

2.5. 4D dose calculation parameters

For all dose calculations, the beam model of PSI-Gantry2 was employed (Pedroni *et al* 2004, Zenklusen *et al* 2010, Safai *et al* 2012) and a uniform dose grid spacing of 2.5 mm^3 was used. Similarly, 4D dose calculations are based on the delivery dynamics of PSI-Gantry2, which are used to calculate the estimated spot delivery sequence. Spot delivery times are calculated assuming 3.5 ms and 4.0 ms for both lateral scanning directions and an energy switching time of 80 ms.

To assess the full influence of motion, we conducted 4D dose calculations without any motion mitigation. Further, we simulated the scenario of volumetric rescanning (VS) performed eight times. These two motion scenarios are denoted as 'VS1' and 'VS8', respectively. Furthermore, as the start of the treatment delivery is usually not synchronized with the respiratory breathing state, which has been shown to influence substantially the dosimetric plan quality (Duetschler *et al* 2023a), 10 equally distributed starting phases in the first breathing cycle were simulated for each 4D dose calculation scenario.

The 4D dose calculations for the three liver and two lung patient cases all included irregular free breathing motion, as provided by the multiple-cycle 4DCT(MRI)s.

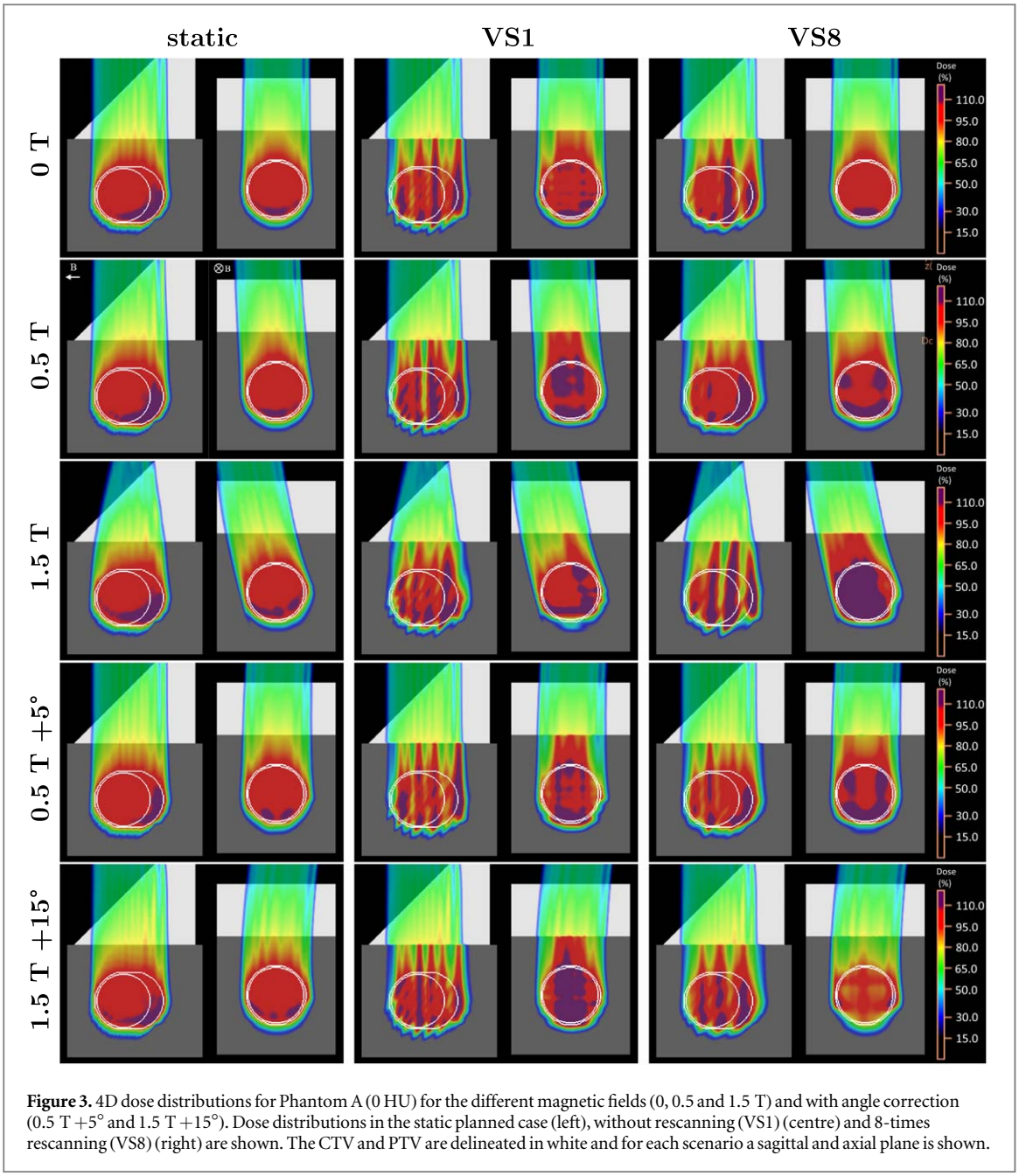

Figure 3. 4D dose distributions for Phantom A (0 HU) for the different magnetic fields (0, 0.5 and 1.5 T) and with angle correction (0.5 T +5° and 1.5 T +15°). Dose distributions in the static planned case (left), without rescanning (VS1) (centre) and 8-times rescanning (VS8) (right) are shown. The CTV and PTV are delineated in white and for each scenario a sagittal and axial plane is shown.

2.6. Plan evaluation

To assess the effects of motion, we compared the 4D dose distributions, which were accumulated on the reference phase, with the static 3D dose distribution as optimized on the planning CT. Additionally, we evaluated dose-volume histograms (DVH) of the reference phase CTV. Further, $V_{95\%}$ and $D_{5\%}$–$D_{95\%}$ within the CTV as measures of target dose coverage and homogeneity were evaluated for each magnetic field strength. Furthermore, the mean dose to the liver or lung surrounding the CTV was studied.

3. Results

3.1. Geometrical phantoms

Static and 4D dose distributions for Phantom A and B are displayed in figures 3 and 4. These dose distributions illustrate the impact of different magnetic field strengths and gantry angle adjustments. As discussed in Duetschler *et al* (2023b), a similar static plan quality is achieved independent of the magnetic field strength. Moreover, a similar plan quality is also achieved when altering the gantry angle to emulate the beam trajectory without magnetic field influence.

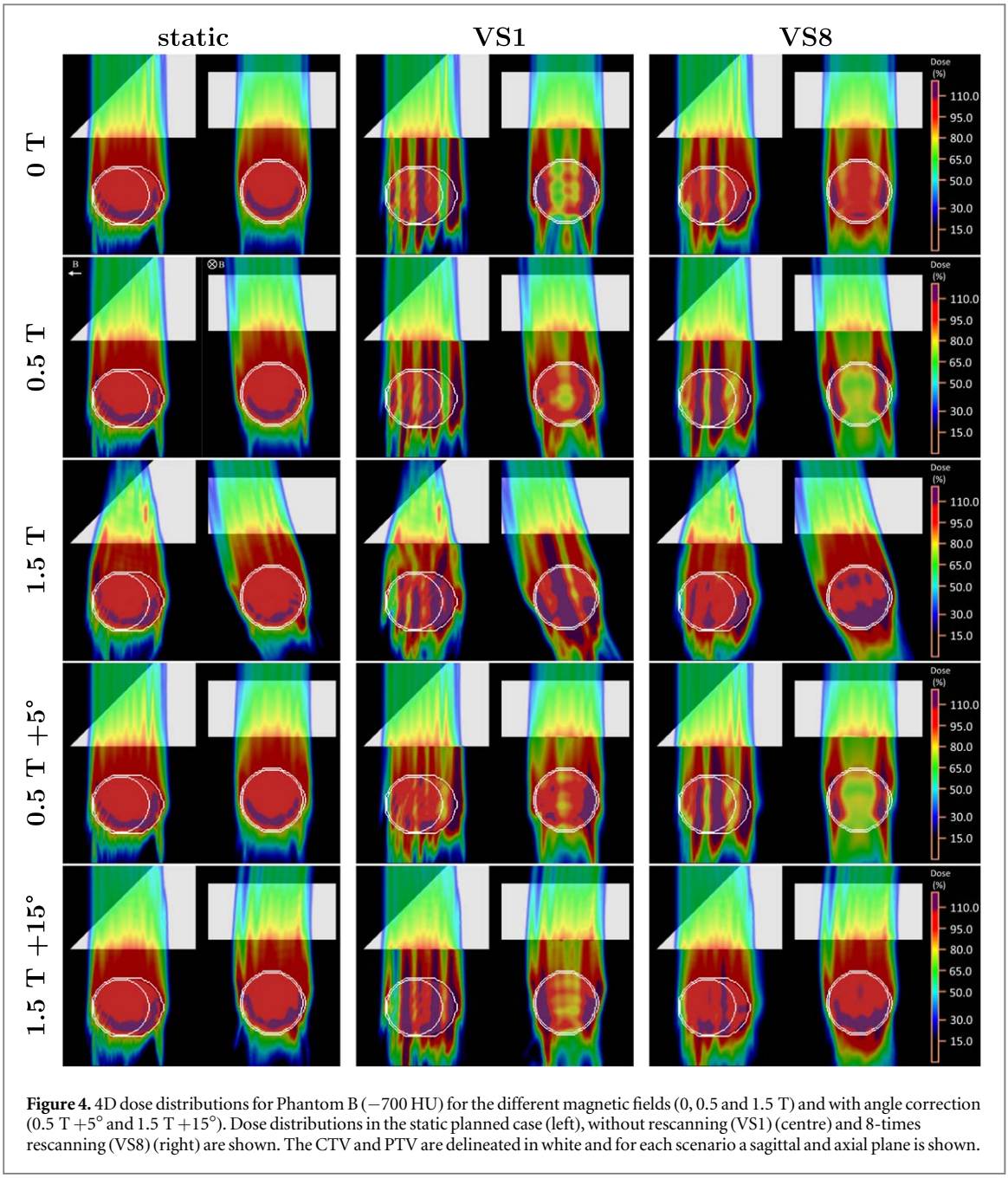

Figure 4. 4D dose distributions for Phantom B (−700 HU) for the different magnetic fields (0, 0.5 and 1.5 T) and with angle correction (0.5 T +5° and 1.5 T +15°). Dose distributions in the static planned case (left), without rescanning (VS1) (centre) and 8-times rescanning (VS8) (right) are shown. The CTV and PTV are delineated in white and for each scenario a sagittal and axial plane is shown.

For all five plans of both phantoms, motion and its induced interplay with the dynamic beam delivery leads to substantial hot and cold spots in the CTV for no rescanning (VS1). This is particularly evident in the sagittal view, while the axial plane highlights the impact of the magnetic field on the treatment plan. For Phantom A 8-times rescanning (VS8), leads to an improvement in the dose coverage and homogeneity for plans with no or low magnetic field, while a further dose degradation can be observed for 1.5 T in figure 3. For phantom B (figure 4), however, both plans with 1.5 T have the best target coverage and homogeneity for simulations with VS8. This is also visible in figure 5, which further shows a comparable impact on the plan quality due to motion (VS1) for 0 T (black), 0.5 T (red) and 1.5 T(blue).

The dose distributions and DVHs in figures 3–5 were calculated assuming the start of the treatment delivery at the start of the first breathing cycle. On the other hand, as the start of the treatment delivery is typically not synchronized with the patient's breathing, the mean values from 10 different starting phases for $V_{95\%}$ and $D_{5\%}$–$D_{95\%}$ for the CTV are listed in tables 1 and 2 for Phantom A and B, respectively. For both geometrical phantoms, the respiratory motion has a similar impact on the CTV dose coverage and homogeneity independent of the magnetic field strength. Furthermore, it should be remarked that even 8-times VS was relatively ineffective as a motion mitigation technique for both studied phantoms and could not restore the CTV dose coverage $V_{95\%}$, which remained well below 95% for all scenarios.

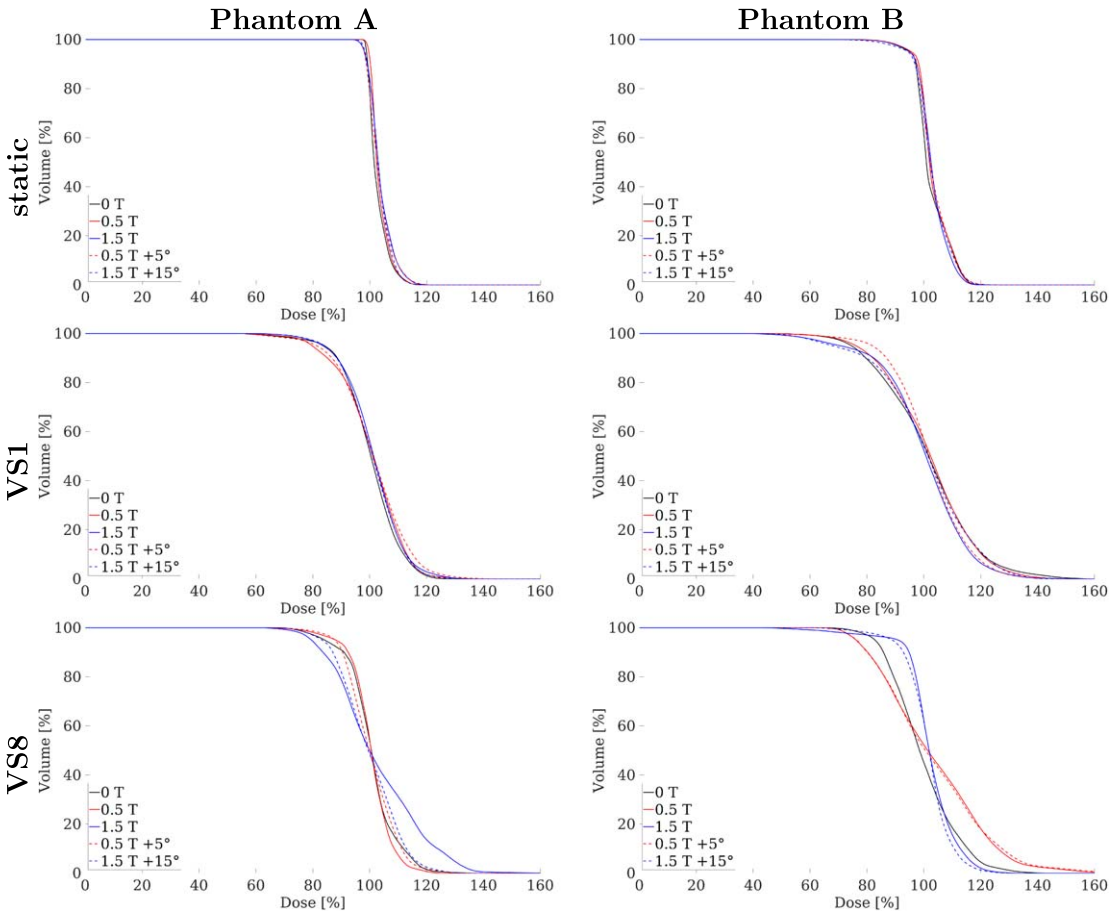

Figure 5. DVHs for CTV of Phantom A (left) and Phantom B (right) for 0 T (black), 0.5 T (red) and 1.5 T (blue). Dashed red and green lines represent plans 0.5 T and 1.5 T with gantry rotated by +5° and +15°, respectively. Results for the static treatment plan (top), no rescanning (middle) and 8-times rescanning (bottom) are shown.

Table 1. DVH parameters for CTV of Phantom A for different magnetic field strengths for the planned static case, without rescanning (VS1) and with 8-times rescanning (VS8) and their differences. For VS1 and VS8 mean values and standard deviation for 10 different starting phases are stated [%].

Magnetic field		Static	VS1	VS1-static	VS8	VS8-static
$V_{95\%}$	0 T	100.0	70.9 ± 2.9	−29.1	76.4 ± 3.4	−23.6
	0.5 T	100.0	73.7 ± 3.8	−26.3	79.6 ± 3.4	−20.4
	1.5 T	99.8	77.0 ± 2.2	−22.8	68.6 ± 8.4	−31.2
	0.5 T + 5°	100.0	73.3 ± 2.8	−26.7	77.8 ± 3.2	−22.2
	1.5 T + 15°	100.0	74.2 ± 2.7	−25.8	67.7 ± 2.3	−32.2
$D_{5\%}$–$D_{95\%}$	0 T	10.8	34.8 ± 2.7	24.0	30.4 ± 4.2	19.6
	0.5 T	10.3	34.4 ± 2.7	24.1	29.5 ± 4.2	19.2
	1.5 T	13.7	32.7 ± 1.7	19.0	38.6 ± 8.0	24.9
	0.5 T + 5°	13.8	36.4 ± 2.7	22.6	31.0 ± 3.6	17.2
	1.5 T + 15°	11.8	34.5 ± 2.4	22.7	35.0 ± 2.3	23.2

3.2. 4DCT(MRI) patient data sets

Dose distributions for two example cases, Liver 1 and Lung 1, are shown in figures 6 and 7. For both cases, comparable static plans are achieved for all three magnetic field strengths and gantry angle corrections of +5 or 15° for 0.5 T and 1.5 T results in comparable beam paths compared to the 0 T plan. The 4D dose distributions without any motion mitigation show pronounced hot and cold spots with different interplay patterns for the different plan configurations. Especially for the Liver 1 case (figure 6), 8-times volumetric rescanning (VS8) restores a mostly homogeneous dose distribution for all five plans. DVHs for these two example cases can be found in figure 8. A plan degradation compared to the static plan for no rescanning can be observed for both cases with the worst CTV coverage for 0 T for Liver 1 and Lung 1. Especially for Liver 1, both plans within a 1.5 T magnetic field result in a better target coverage for VS1.

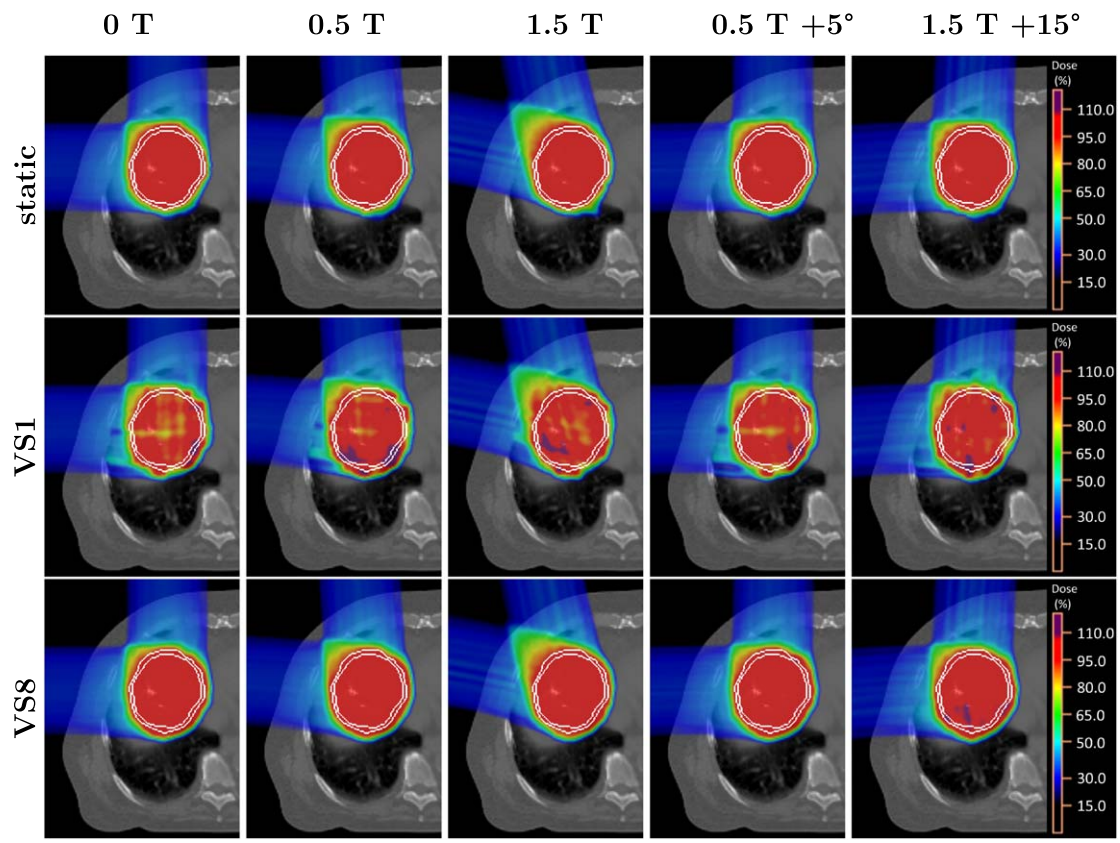

Figure 6. 4D dose distributions for Liver 1 for the different magnetic fields (0, 0.5 and 1.5 T) and with angle correction (0.5 T +5° and 1.5 T +15°). Dose distributions in the static planned case (top), without rescanning (VS1) (middle) and 8-times rescanning (VS8) (bottom) are shown. The CTV and PTV are delineated in white.

Table 2. DVH parameters for CTV of Phantom B for different magnetic field strengths for the planned static case, without rescanning (VS1) and with 8-times rescanning (VS8) and their differences. For VS1 and VS8 mean values and standard deviation for 10 different starting phases are stated [%].

Magnetic field	Static	VS1	VS1-static	VS8	VS8-static	
$V_{95\%}$	0 T	95.0	68.8 ± 2.8	−26.2	68.7 ± 5.0	−26.2
	0.5 T	95.4	67.7 ± 3.5	−27.7	69.1 ± 8.8	−26.4
	1.5 T	95.1	70.2 ± 4.0	−25.0	71.0 ± 9.3	−24.1
	0.5 T + 5°	95.2	70.3 ± 2.1	−25.0	69.1 ± 9.3	−26.2
	1.5 T + 15°	94.4	69.1 ± 2.7	−25.3	79.4 ± 4.7	−15.0
$D_{5\%}$–$D_{95\%}$	0 T	19.2	49.6 ± 5.0	30.4	37.2 ± 3.4	18.1
	0.5 T	18.2	51.6 ± 6.3	33.4	44.3 ± 10.5	26.1
	1.5 T	17.8	49.6 ± 5.7	31.8	40.5 ± 8.5	22.8
	0.5 T + 5°	18.9	50.7 ± 4.4	31.8	45.2 ± 10.8	26.3
	1.5 T + 15°	20.0	52.3 ± 4.9	32.3	33.7 ± 5.0	13.7

Figure 9 summarizes the results for all five 4DCT(MRI)s and using different starting phases for the delivery simulations. Apart from Liver 3, respiratory motion (VS1) results in a more pronounced degradation of the CTV dose coverage $V_{95\%}$ for plans without any magnetic field than for 1.5 T (see figure 9(a)). On average a decrease of $V_{95\%}$ of the CTV for VS1 compared to the static case of 19.9% was observed for the 0 T plan. A smaller decrease in the CTV coverage $V_{95\%}$ of 17.0% (17.7%) was observed for the 1.5 T (+15°) plan. Also 0.5 T (+5°) resulted in on average slightly smaller differences in $V_{95\%}$ due to motion of 18.9% (17.4%). The average increase in CTV $D_{5\%}$–$D_{95\%}$ from the static plan due to motion is also slightly reduced for the 1.5 T plans (16.8% and 17.7%) compared to the 0 T plan (18.2%). However, larger average differences occur for 0.5 T (19.0% and 18.6%). In summary, across all five analysed cases, we observed a comparable effect on CTV dose coverage and homogeneity caused by motion, irrespective of the magnetic field strength.

8-times rescanning results in improved target dose coverage and homogeneity. For 0 T, an average difference to the static plan of −4.9% and 5.8% in $V_{95\%}$ and $D_{5\%}$–$D_{95\%}$ in the CTV has been found. Calculations with a

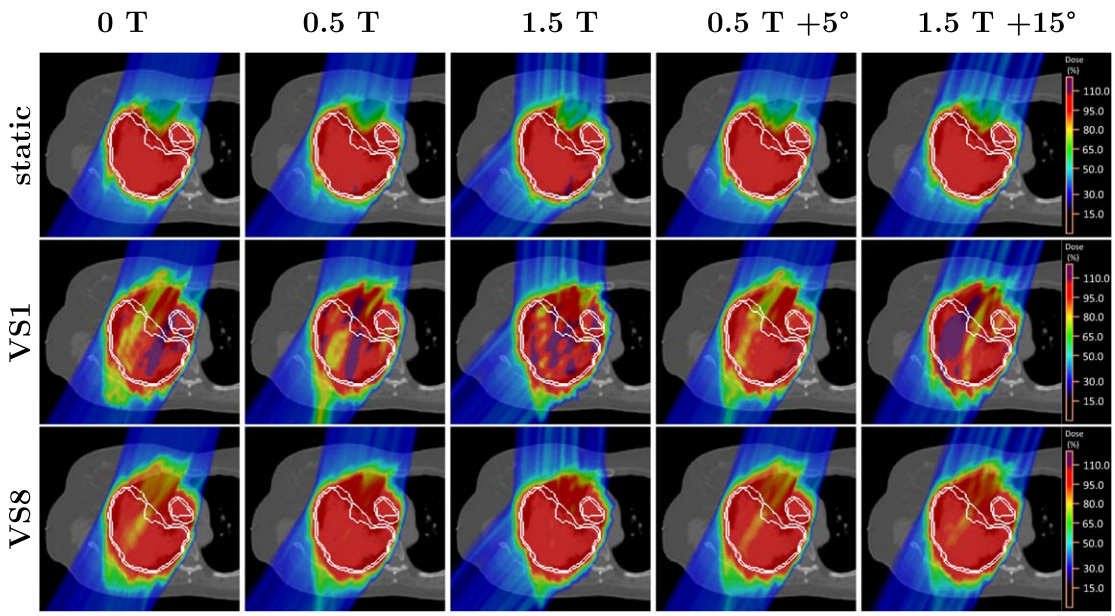

Figure 7. 4D dose distributions for Lung 1 for the different magnetic fields (0, 0.5 and 1.5 T) and with angle correction (0.5 T +5° and 1.5 T +15°). Dose distributions in the static planned case (top), without rescanning (VS1) (middle) and 8-times rescanning (VS8) (bottom) are shown. The CTV and PTV are delineated in white.

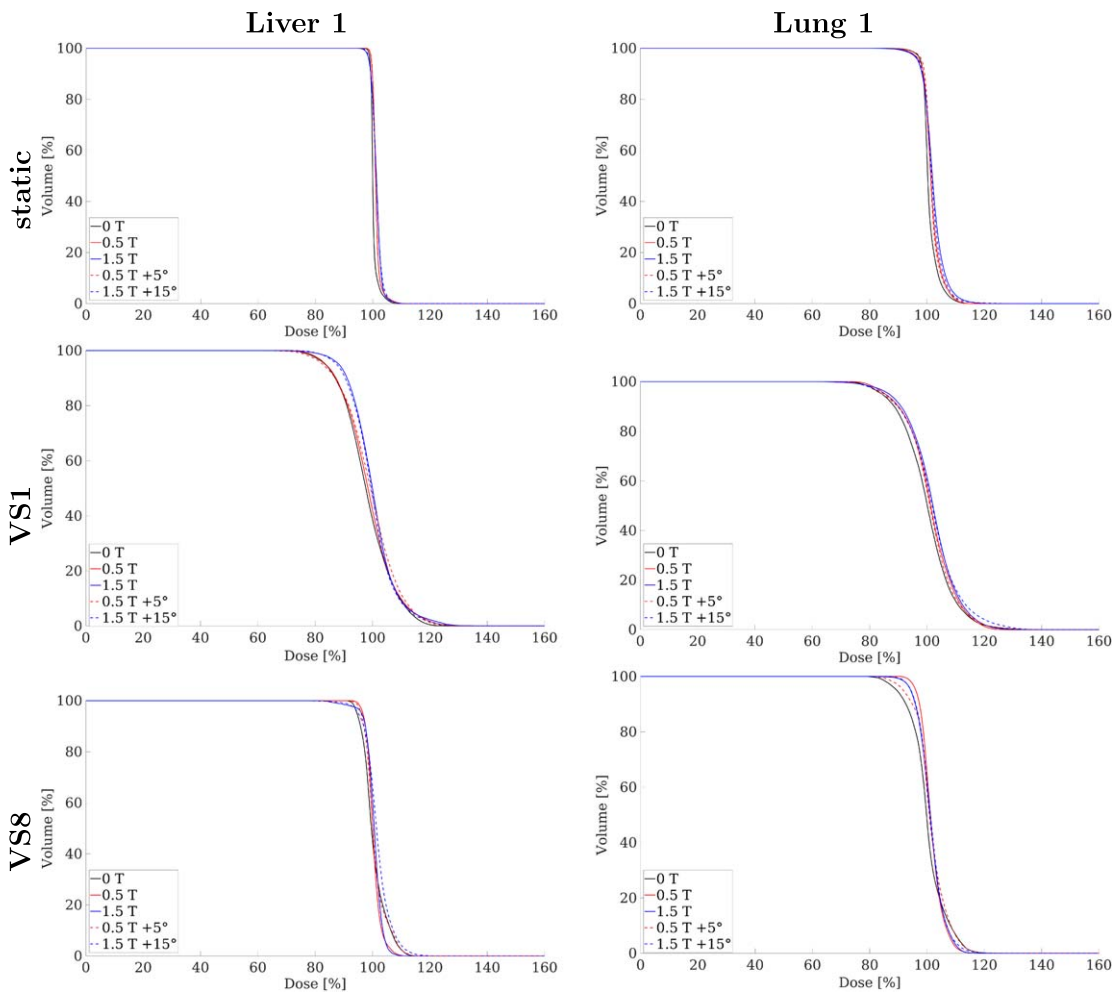

Figure 8. DVHs for CTV of Liver 1 (left) and Lung 1 (right) for 0 T (black), 0.5 T (red) and 1.5 T (blue). Dashed red and green lines represent plans 0.5 T and 1.5 T with gantry rotated by +5° and +15°, respectively. Results for the static treatment plan (top), no rescanning (middle) and 8-times rescanning (bottom) are shown.

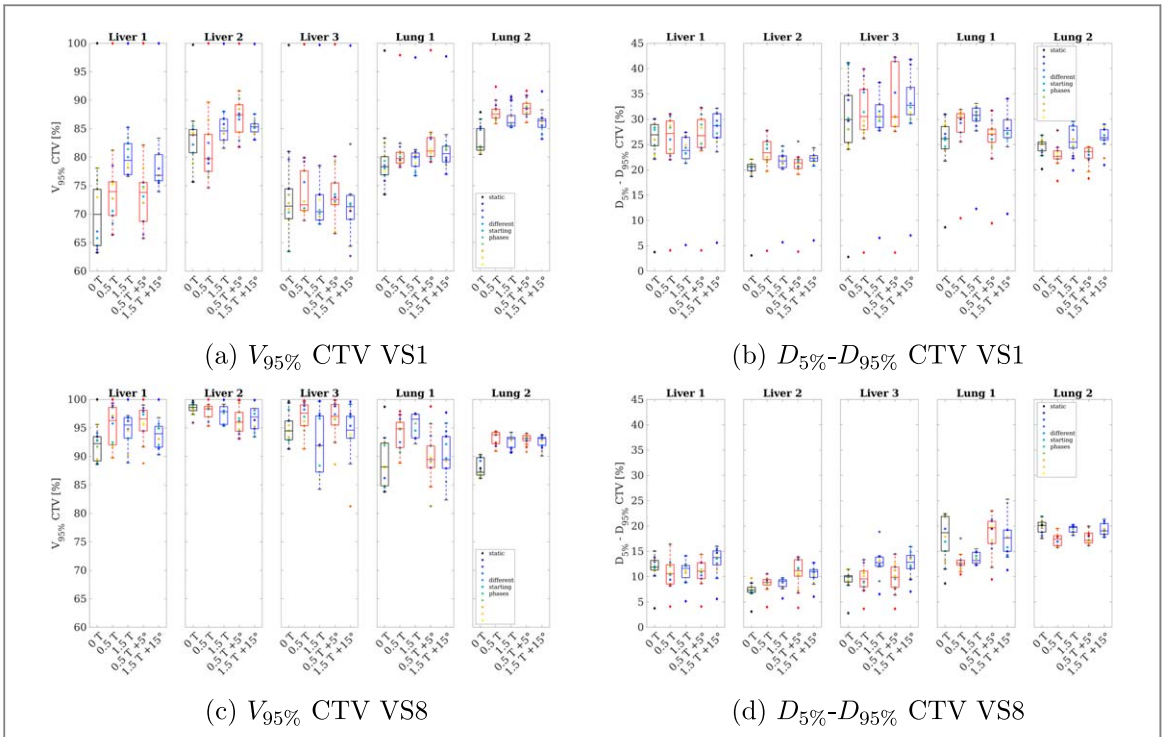

Figure 9. Boxplots of $V_{95\%}$ (left) and $D_{5\%}$–$D_{95\%}$ (right) for the CTV showing the impact of 10 different starting phases for no rescanning (top) and 8-times volumetric rescanning (bottom). The diamonds mark the values of the static plans, while different coloured circles show the dosimetric indices for different starting phases (a) $V_{95\%}$ CTV VS1 (b) $D_{5\%}$–$D_{95\%}$ CTV VS1 (c) $V_{95\%}$ CTV VS8 (d) $D_{5\%}$–$D_{95\%}$ CTV VS8.

magnetic field result in average differences compared to the static plan in the range of −2.6% (0.5 T) and −4.5% (1.5 T +15°) for the CTV coverage $V_{95\%}$. Average differences in the CTV homogeneity $D_{5\%}$–$D_{95\%}$ range between 3.3% (1.5 T) and 5.9% (0.5 T +5°). It should further be remarked that especially for the two lung cases with pronounced density heterogeneities, an acceptable target coverage ($V_{95\%} > 95\%$) could not be restored in our simulations, even with VS8.

For normal tissue doses, respiratory motion resulted in differences up to 5.9% in the mean dose to the surrounding liver/lung compared to the static plan. The impact of motion was comparable for all planning scenarios and independent of the magnetic field. The different beam trajectories introduced by the magnetic field also only resulted in small differences in the static mean liver/lung dose up to 1%.

4. Discussion

To the best of our knowledge, this paper represents the first study into the combined impact of magnetic fields and motion on PBS proton therapy dose distributions. Our analysis of the studied configurations revealed that the influence of motion on treatment plans was similar both with and without the presence of a magnetic field. Thus, our work provides valuable evidence that MRI-guided proton therapy, with adequate motion management, could be considered as an option for treating mobile tumours using similar motion mitigation methods as for normal PBS proton therapy, i.e. rescanning as studied here. Furthermore, for some of the studied cases, the plans optimised in the presence of a magnetic field were even slightly less affected by the respiratory motion. A possible explanation could be the planning strategy used in this study, where spot positions were shifted according to an energy-specific lateral scanning shift before the optimisation considering the magnetic field (Duetschler *et al* 2023b). Thus, while for plans without any magnetic field spots are placed on a regular rectilinear grid, this grid is distorted in the presence of a magnetic field due to the different materials in the beam path. It should, however, be further investigated, whether a slightly irregular spot placement could result in treatment plans which are more robust to respiratory motion and further cases should be investigated.

The effect of motion on the dosimetric plan quality can be greatly influenced by the proton beam direction (Knopf *et al* 2011, Chang *et al* 2017). Our treatment planning strategy results not only in a different deflected beam trajectory within the patient but also in an apparent difference in the beam entrance. As this could influence the impact of motion, additional treatment plans with +5° and +15° gantry rotations for 0.5 and 1.5T were generated and used to also study the impact of motion. The angles were manually selected for both

magnetic field strength and could correct for the beam deflection and generate very similar treatment plans than without any magnetic field. Manually tuned gantry angle corrections were also used by Kurz *et al* (2017) for investigating the treatment plan robustness of MRI-guided proton therapy treatment plans. Instead of a manual gantry angle correction, Burigo and Oborn (2021) have also suggested automatic methods minimizing the mean path difference within the patient compared to the straight dose deposition without magnetic field. In this study, no substantial differences in the interplay effect with or without gantry angle correction could be observed. However, the different beam trajectories could result in significantly different dose distributions to critical nearby OARs.

In this work, the magnetic field was directed along the most pronounced SI direction of motion. The magnetic field perpendicular to the beam direction thus results in a deflection perpendicular to the main motion axis. This setup is motivated by the assumption that the patient would be treated in supine within the bore of an MRI. Recently, there has however been growing interest in upright patient positioning (Volz *et al* 2022). This could considerably reduce the costs associated with MRI-guided proton therapy, which could be implemented using a fixed horizontal beamline and an open-bore MRI with an upright patient positioning system to rotate the patient. Indeed, this is one of the motivations for investigating here the effects on plans with a 0.5 T magnetic field. For such a setup the magnetic field would be perpendicular to the SI motion direction. Different relative orientations of motion, proton beam and perpendicular magnetic field were investigated in a preliminary study, in which no significant differences could be observed. However, different configurations should be investigated separately before clinical use.

Most 4D dose calculation algorithms used for PBS proton therapy are based on warping and accumulating dose contributions to the different phases of a 4DCT. The temporal resolution of the 4D dose calculation is thus given by the temporal resolution of the 4DCT, which can be much coarser than the time between the delivery of two spots. A finer temporal resolution can be achieved using the deforming dose grid algorithm (Boye *et al* 2013a, Krieger *et al* 2018, Zhang *et al* 2019), which deforms the dose calculation grid according to the DVFs extracted from the 4DCT. The DVFs can then be interpolated in time for a finer (sub-)spot-wise dose calculation. Depending on the motion period, delivery dynamics and fractionation dose the temporal resolution can result in substantial dosimetric differences (Zhang *et al* 2019). Indeed, the 4DCT(MRI) cases used in this study have previously been used to investigate the limitations of phase-sorting 4D dose calculation (Duetschler *et al* 2023a). In that study, only a small dosimetric impact due to the temporal resolution of the 4D dose calculation was found. Consequently, a dose warping approach was chosen in this study, but a combination with the deforming dose grid algorithm is envisaged in future developments. In the same study, it was also shown that neglecting variations in respiratory motion can lead to a substantial underestimation of dosimetric motion effect. Thus, in this study, 4D dose calculations were performed for multiple-cycle 4DCT(MRI)s, which reflect free breathing motion. It should further be remarked, that one of the lung 4DCT(MRI)s used in Duetschler *et al* (2023a) was excluded for the present study. This is due to the current limitations of the analytical dose calculation algorithm in the presence of magnetic fields (Duetschler *et al* 2023b), which does not support the use of pre-absorbers, which would be necessary to achieve an acceptable target coverage for that case.

For better comparability, we chose to use the same planning target definition for treatment plans optimised with and without magnetic fields. Furthermore, positioning errors were not simulated, Fuchs *et al* (2017) however have previously shown similar robustness of treatment plans with and without magnetic field. On the other hand, the superior soft-tissue contrast of MRI-guided PBS proton therapy could result in more accurate patient positioning and the consequently reduced margins could result in better sparing of healthy tissue and OARs. Furthermore, MRI guidance could result in improved accuracy of other motion mitigation techniques, such as breath-hold, gating or tracking, which usually rely on internal or external surrogates. For instance, online cine-MRI could provide direct information about the tumour and surrounding anatomy in real-time.

5. Conclusion

We have presented the first study of the combined effects of magnetic fields and respiratory motion on the dose for PBS proton therapy. For the studied cases, with the magnetic field parallel to the most pronounced motion along the SI direction and perpendicular to the incident proton beams, a similar dosimetric effect due to motion was observed regardless of magnetic field strength. Depending on the planning strategy, the presence of a magnetic field could even slightly increase the robustness of the treatment plan to motion.

Acknowledgments

This project is funded by the Swiss Cancer Research Foundation (KFS-4517-08-2018).

Data availability statement

The data cannot be made publicly available upon publication because they contain sensitive personal information. The data that support the findings of this study are available upon reasonable request from the authors.

Conflict of interest

The authors report no conflict of interest.

ORCID iDs

Alisha Duetschler https://orcid.org/0000-0001-5121-8032
Ye Zhang https://orcid.org/0000-0003-1608-4467

References

Acharya S, Wang C, Quesada S, Gargone M A, Ates O, Uh J, Krasin M J, Merchant T E and Hua C h 2020 Adaptive proton therapy for pediatric patients: improving the quality of the delivered plan with on-treatment MRI *Int. J. Radiat. Oncol. Biol. Phys.* **109** P242–251

Botas P, Grassberger C, Sharp G and Paganetti H 2018 Density overwrites of internal tumor volumes in intensity modulated proton therapy plans for mobile lung tumors *Phys. Med. Biol.* **63** 035023

Boye D, Lomax T and Knopf A 2013a Mapping motion from 4D-MRI to 3D-CT for use in 4D dose calculations: a technical feasibility study *Med. Phys.* **40** 61702

Bragg W H and Kleeman R 1905 XXXIX. On the α particles of radium, and their loss of range in passing through various atoms and molecules *London Edinburgh Dublin Phil. Mag. J. Sci.* **10** 318–40

Burigo L N and Oborn B M 2019 MRI-guided proton therapy planning: accounting for an inline MRI fringe field *Phys. Med. Biol.* **64** 215015

Burigo L N and Oborn B M 2021 Integrated MRI-guided proton therapy planning: accounting for the full MRI field in a perpendicular system *Med. Phys.* (https://doi.org/10.1002/mp.15398)

Chang J Y *et al* 2017 Consensus guidelines for implementing pencil-beam scanning proton therapy for thoracic malignancies on behalf of the PTCOG thoracic and lymphoma subcommittee *Int. J. Radiat. Oncol. Biol. Phys.* **99** 41–50

Duetschler A, Prendi J, Safai S, Weber D C, Lomax A J and Zhang Y 2023a Limitations of phase-sorting based pencil beam scanned 4D proton dose calculations under irregular motion *Phys. Med. Biol.* **68** 015015

Duetschler A, Winterhalter C, Meier G, Safai S, Weber D C, Lomax A J and Zhang Y 2023b A fast analytical dose calculation approach for MRI-guided proton therapy *Phys. Med. Biol.* **68** 195020

Duetschler A *et al* 2022 Synthetic 4DCT(MRI) lung phantom generation for 4D radiotherapy and image guidance investigations *Med. Phys.* **49** 2890–903

Faddegon B, Ramos-Mendez J, Schuemann J, McNamara A, Shin J, Perl J and Paganetti H 2020 The TOPAS tool for particle simulation, a Monte Carlo simulation tool for physics, biology and clinical research *Phys. Med.* **72** 114–21

Fuchs H, Moser P, Gröschl M and Georg D 2017 Magnetic field effects on particle beams and their implications for dose calculation in MR-guided particle therapy *Med. Phys.* **44** 1149–56

Fuchs H, Padilla-Cabal F, Oborn B M and Georg D 2022 Commissioning a beam line for MR-guided particle therapy assisted by in silico methods *Med. Phys.* (https://doi.org/10.1002/mp.16143)

Gantz S, Hietschold V and Hoffmann A L 2020 Characterization of magnetic interference and image artefacts during simultaneous in-beam MR imaging and proton pencil beam scanning *Phys. Med. Biol.* **65** 215014

Gantz S, Schellhammer S M and Hoffmann A L 2021 Image performance characterization of an in-beam low-field magnetic resonance imaging system during static proton beam irradiation *IEEE Trans. Radiat. Plasma Med. Sci.* **6** 271–81

Hartman J, Kontaxis C, Bol G H, Frank S J, Lagendijk J J W, van Vulpen M and Raaymakers B W 2015 Dosimetric feasibility of intensity modulated proton therapy in a transverse magnetic field of 1.5 T *Phys. Med. Biol.* **60** 5955–69

Hoffmann A *et al* 2020 MR-guided proton therapy: a review and a preview *Radiat. Oncol.* **15** 129

Josipovic M, Persson G F, Dueck J, Bangsgaard J P, Westman G, Specht L and Aznar M C 2016 Geometric uncertainties in voluntary deep inspiration breath hold radiotherapy for locally advanced lung cancer *Radiother. Oncol.* **118** 510–4

Jud C, Nguyen D, Sandkühler R, Giger A, Bieri O and Cattin P C 2018 Motion aware MR imaging via spatial core correspondence *Lecture Notes in Computer Science* ed A F Frangi *et al* (Cham: Springer) (*Lecture Notes in Artificial Intelligence and Lecture Notes in Bioinformatics*) vol 11070 LNCS, pp 198–205

Knopf A C, Hong T S and Lomax A 2011 Scanned proton radiotherapy for mobile targets—The effectiveness of re-scanning in the context of different treatment planning approaches and for different motion characteristics *Phys. Med. Biol.* **56** 7257–71

Krieger M, Klimpki G, Fattori G, Hrbacek J, Oxley D, Safai S, Weber D C, Lomax A J and Zhang Y 2018 Experimental validation of a deforming grid 4D dose calculation for PBS proton therapy *Phys. Med. Biol.* **63** 055005

Kurz C, Landry G, Resch A F, Dedes G, Kamp F, Ganswindt U, Belka C, Raaymakers B W and Parodi K 2017 A Monte Carlo study to assess the effect of 1.5 T magnetic fields on the overall robustness of pencil-beam scanning proton radiotherapy plans for prostate cancer *Phys. Med. Biol.* **62** 8470–82

Lomax A J, Bortfeld T, Goitein G, Debus J, Dykstra C, Tercier P A, Coucke P A and Mirimanoff R O 1999a A treatment planning inter-comparison of proton and intensity modulated photon radiotherapy *Radiother. Oncol.* **51** 257–71

Lühr A, Burigo L N, Gantz S, Schellhammer S M and Hoffmann A L 2019 Proton beam electron return effect: Monte Carlo simulations and experimental verification *Phys. Med. Biol.* **64** 035012

Moteabbed M, Harisinghani M, Paganetti H, Trofimov A, Lu H-M and Efstathiou J A 2021b Proton versus photon radiotherapy for MR-guided dose escalation of intraprostatic lesions *Acta Oncol.* **60** 1283–90

Moteabbed M, Schuemann J and Paganetti H 2014 Dosimetric feasibility of real-time MRI-guided proton therapy *Med. Phys.* **41** 111713

Moteabbed M, Smeets J, Hong T S, Janssens G, Labarbe R, Wolfgang J A and Bortfeld T R 2021a Toward MR-integrated proton therapy: modeling the potential benefits for liver tumors *Phys. Med Biol.* **66** 195004
Mutic S and Dempsey J F 2014 The ViewRay system: magnetic resonance-guided and controlled radiotherapy *Semin. Radiat. Oncol.* **24** 196–9
Oborn B M, Dowdell S, Metcalfe P E, Crozier S, Mohan R and Keall P J 2015 Proton beam deflection in MRI fields: implications for MRI-guided proton therapy *Med. Phys.* **42** 2113–24
Oborn B M, Dowdell S, Metcalfe P E, Crozier S, Mohan R and Keall P J 2017 Future of medical physics: real-time MRI-guided proton therapy *Med. Phys.* **44** e77–90
Padilla-Cabal F, Alejandro Fragoso J, Franz Resch A, Georg D and Fuchs H 2020 Benchmarking a GATE/Geant4 Monte Carlo model for proton beams in magnetic fields *Med. Phys.* **47** 223–33
Padilla-Cabal F, Georg D and Fuchs H 2018 A pencil beam algorithm for magnetic resonance image-guided proton therapy *Med. Phys.* **45** 2195–204
Padilla-Cabal F, Kuess P, Georg D, Palmans H, Fetty L and Fuchs H 2019 Characterization of EBT3 radiochromic films for dosimetry of proton beams in the presence of magnetic fields *Med. Phys.* **46** 3278–84
Pedroni E *et al* 2004 The PSI Gantry 2: a second generation proton scanning gantry *Z. Med. Phys.* **14** 25–34
Perl J, Shin J, Schumann J, Faddegon B and Paganetti H 2012 TOPAS: an innovative proton Monte Carlo platform for research and clinical applications *Med. Phys.* **39** 6818
Pham T T, Whelan B, Oborn B M, Delaney G P, Vinod S, Brighi C, Barton M and Keall P 2022 Magnetic resonance imaging (MRI) guided proton therapy: a review of the clinical challenges, potential benefits and pathway to implementation *Radiother. Oncol.* **170** 37–47
Raaymakers B W, Raaijmakers A J E and Lagendijk J J W 2008 Feasibility of MRI guided proton therapy: magnetic field dose effects *Phys. Med. Biol.* **53** 5615–22
Raaymakers B W *et al* 2017 First patients treated with a 1.5 T MRI-Linac: clinical proof of concept of a high-precision, high-field MRI guided radiotherapy treatment *Phys. Med. Biol.* **62** L41–50
Rabe M, Palacios M A, van Sörnsen de Koste J R, Eze C, Hillbrand M, Belka C, Landry G, Senan S and Kurz C 2023 Comparison of MR-guided radiotherapy accumulated doses for central lung tumors with non-adaptive and online adaptive proton therapy *Med. Phys.* **50** 2625–36
Safai S, Bula C, Meer D and Pedroni E 2012 Improving the precision and performance of proton pencil beam scanning *Trans. Cancer Res.* **1** 196–206
Santos D M, Wachowicz K, Burke B and Fallone B G 2019 Proton beam behavior in a parallel configured MRI-proton therapy hybrid: effects of time-varying gradient magnetic fields *Med. Phys.* **46** 822–38
Schaffner B, Pedroni E and Lomax A 1999 Dose calculation models for proton treatment planning using a dynamic beam delivery system: an attempt to include density heterogeneity effects in the analytical dose calculation *Phys. Med. Biol.* **44** 27–41
Schellhammer S M, Gantz S, Lühr A, Oborn B M, Bussmann M and Hoffmann A L 2018b Technical Note: experimental verification of magnetic field-induced beam deflection and Bragg peak displacement for MR-integrated proton therapy *Med. Phys.* **45** 3429–34
Schellhammer S M and Hoffmann A L 2017 Prediction and compensation of magnetic beam deflection in MR-integrated proton therapy: a method optimized regarding accuracy, versatility and speed *Phys. Med. Biol.* **62** 1548–64
Schellhammer S M, Hoffmann A L, Gantz S, Smeets J, van der Kraaij E, Quets S, Pieck S, Karsch L and Pawelke J 2018a Integrating a low-field open MR scanner with a static proton research beam line: proof of concept *Phys. Med. Biol.* **63** 23LT01
Volz L, Sheng Y, Durante M and Graeff C 2022 Considerations for upright particle therapy patient positioning and associated image guidance *Front. Oncol.* **12** 3430
von Siebenthal M, Székely G, Gamper U, Boesiger P, Lomax A and Cattin P 2007 4D MR imaging of respiratory organ motion and its variability *Phys. Med. Biol.* **52** 1547–64
Wolf R and Bortfeld T 2012 An analytical solution to proton Bragg peak deflection in a magnetic field *Phys. Med. Biol.* **57** N329–37
Zenklusen S M, Pedroni E and Meer D 2010 A study on repainting strategies for treating moderately moving targets with proton pencil beam scanning at the new gantry 2 at PSI *Phys. Med. Biol.* **55** 5103–21
Zhang Y, Huth I, Weber D C and Lomax A J 2019 Dosimetric uncertainties as a result of temporal resolution in 4D dose calculations for PBS proton therapy *Phys. Med. Biol.* **64** 125005